JOURNAL OF PROPULSION AND POWER
Vol. 21, No. 1, January–February 2005

Comparison of Detonation Processes in a Variable Cross Section Chamber and a Simple Tube

H. Y. Fan* and F. K. Lu†
University of Texas at Arlington, Arlington, Texas 76019-0018

The detonation processes occurring in a variable cross section detonation chamber are compared with that occurring in a simple, constant cross section tube. The variable cross section chamber is made up of a large tube and two small identical tubes connected on each side through frustums. The simple tube has the same diameter as the small tubes of the variable cross section chamber and the same total length as the entire variable section chamber. Both channels are closed at the left end and opened at the right. A two-dimensional, time-accurate, finite volume-based method is used to perform the computations. A five-species, two-step global hydrogen–air reaction mechanism is used. The study showed complex wave phenomena in the variable cross section chamber that have an impact on thrust and specific impulse.

I. Introduction

PULSE detonation engines (PDEs) have recently been recognized as a promising propulsion technology that offers advantages in thermodynamic cycle efficiency, hardware simplicity, scalability, and reliability. PDEs use detonation combustion rather than deflagration to produce rapid energy release and high specific power. Such engines operate on an intermittent cycle by filling a chamber with reactants and inducing ignition in an energetic fashion such that a detonation wave is rapidly established.[1–3] The high propagation speed of the detonation wave yields a large increase in combustion rates relative to the deflagration mode, and the chemical energy is completely released within a narrow region behind the leading shock wave. Consequently, the combustion process takes place at nearly constant volume, which yields a higher postcombustion temperature than a constant pressure process. In recent years, numerous researchers have studied PDEs through experiments[4–10] or analytical and numerical analyses,[11–20] and various configurations have been proposed. An excellent technical overview of the development of the PDEs is provided by Kailasanath.[1] Overviews of past and ongoing numerical simulations of PDEs are well described by Kailasanath1[1,21,22] and He and Karagozian.[20]

Most PDE studies, both experimental and numerical, to date have been performed on simple configurations, namely, with tubes of constant cross section.[1] Baklanov et al.[23] and Baklanov and Gvozdeva[24,25] performed an experimental study of detonation with variable cross section chambers. They found the possibility of producing flow parameters more extreme than those behind a stationary detonation wave. Besides the cited experimental study, no other studies, including numerical ones, have been reported on such a configuration. Recently, a numerical study was performed by the authors on the detonation processes occurring in a variable cross section chamber for a hydrogen–air reactive flow.[26] The study emphasized the detonation phenomena appearing in a given variable cross section chamber. The results obtained from the study supported the experimental observations by Baklanov et al.[23] and also provided further insight into the complex wave phenomena in the variable chamber configuration.

A numerical study was performed to understand further the detonation phenomena that occurs in a variable cross section configuration, as compared to those occurring in a simple tube. The configuration of the variable cross section chamber is chosen as that of Ref. 26. The chamber is made up of a large tube and two small identical tubes connected on each side through frustums. The simple tube is assumed to have the same diameter as the small tube of the variable cross section chamber. The two channels have the same total length. A two-dimensional, time-accurate, finite volume-based method that was developed for hydrogen–air combustion[27] is used to perform the numerical simulation of the detonation processes that are governed by Euler equations and a five-species, two-step hydrogen–air combustion mechanism.

II. Problem Formulation and Numerical Method

The numerical technique was previously reported by Kim et al.,[27] and only a summary is provided here. The time-dependent two-dimensional Euler equations are used to describe an inviscid, non-heat-conducting, reacting gas flow in which thermal nonequilibrium is modeled with a two-temperature model. These equations can be expressed in Cartesian coordinates as

$$\frac{\partial \boldsymbol{U}}{\partial t} + \frac{\partial \boldsymbol{F}}{\partial x} + \frac{\partial \boldsymbol{G}}{\partial y} = \boldsymbol{S} \tag{1}$$

where $\boldsymbol{U}$ is the vector of conserved variables, $\boldsymbol{F}$ and $\boldsymbol{G}$ are the convective flux vectors, and $\boldsymbol{S}$ is the vector of source terms:

$$\boldsymbol{U} = \begin{bmatrix} \rho_s \\ \rho u \\ \rho v \\ \rho e_v \\ \rho E \end{bmatrix}, \qquad \boldsymbol{F} = \begin{bmatrix} \rho_s u \\ \rho u^2 + p \\ \rho u v \\ \rho u e_v \\ \rho u E + p u \end{bmatrix}$$

$$\boldsymbol{G} = \begin{bmatrix} \rho_s v \\ \rho u v \\ \rho v^2 + p \\ \rho v e_v \\ \rho v E + p v \end{bmatrix}, \qquad \boldsymbol{S} = \begin{bmatrix} w_s \\ 0 \\ 0 \\ w_v \\ 0 \end{bmatrix} \tag{2}$$

The subscript $s = 1, 2, 3, \ldots, N_s$, where N_s is the number of species. The first N_s rows represent species continuity, followed by the two momentum conservation equations for the mixture. The next row describes the rate of change in the vibrational energy, and the final row is the total energy conservation equation. The terms u and v are

---

Received 5 November 2003; revision received 16 August 2004; accepted for publication 16 August 2004.

*Visiting Researcher, Aerodynamics Research Center, Mechanical and Aerospace Engineering Department.

†Professor and Director, Aerodynamics Research Center, Mechanical and Aerospace Engineering Department. Associate Fellow AIAA.

the velocities in the x and y directions, respectively,

$$\rho = \sum_{s=1}^{N_s} \rho_s$$

is the mixture density, ρ_s is the density of species s, p is the pressure, e_v is the vibrational energy, E is the total energy per unit mass of mixture, w_s is the mass of production rate of species s per unit volume, and w_v is the vibrational energy source.

The internal energy based on the two-temperature model is assumed to comprise an equilibium portion at the translational temperature T and a nonequilibium portion at the vibrational temperature T_v and can be defined as

$$e = e_{\text{eq}}(T) + e_v(T_v) \tag{3}$$

These energy components can be determined with certain thermodynamic relations.

The source terms for the species mass production rate in the chemical reactions can be written as

$$w_s = M_s \sum_{r=1}^{N_r} (\beta_{s,r} - \alpha_{s,r})(R_{f,r} - R_{b,r}) \tag{4}$$

where M_s is the molecular weight of species s, N_r is the number of reactions, and $\alpha_{s,r}$ and $\beta_{s,r}$ are the stoichiometric coefficients for reactants and products, respectively, in the rth reaction. The forward and backward reaction rates of the rth reaction are $R_{f,r}$ and $R_{b,r}$ respectively. These rates can be determined by the Arrhenius law. The source term of vibrational energy can be written as

$$w_v = \sum_s Q_{v,s} + \sum_s w_s e_{v,s} \tag{5}$$

The first term on the right hand side, $Q_{v,s}$, represents the vibrational energy exchange rate of species s due to the relaxation process with translational energy, which can be determined by the Landau–Teller formulation (see Refs. 28 and 29). The second term, $w_s e_{v,s}$, represents the amount of vibrational energy gained or lost due to production or depletion of species s from chemical reactions.

In the current study, the Rogers–Chinitz[30] hydrogen-air combustion mechanism of five-species (N_2, O_2, H_2, H_2O, and OH) and two-reactions ($H_2 + O_2 = 2OH$ and $2OH + H_2 = 2H_2O$) is used. This model was developed to represent hydrogen–air chemical kinetics with as few reaction steps as possible while still giving reasonably accurate global results. In this model, nitrogen is counted as a collisional partner in the thermodynamic model and relaxation process, but is not included in the chemical reaction model because the maximum temperature in the hydrogen–air reaction does not reach the dissociation temperature of nitrogen.

A finite volume algorithm was used to solve the preceding equations numerically. The advantage of this method is its use of the integral form of the equations, which ensures conservation and which allows the correct treatment of discontinuities. Nonequilibrium flows involving finite-rate chemistry and thermal energy relaxation often can be very difficult to solve numerically because of stiffness. The present method includes a point implicit treatment of source terms to reduce the inherent stiffness of the system by effectively rescaling all of the characteristic times in the fields into the same order of magnitude. A local ignition averaging model (LIAM) is further taken to handle the additional stiffness in the ignition cells. The basic idea for this model comes from the fact that the species mass fractions are changing drastically in a very short period with ignition but reaches equilibrium soon afterward. LIAM separates the cell in which the ignition condition is met and then integrates the chemical kinetics equations alone in that cell with a time step much smaller than the flow solver time step. Temporal accuracy is improved by using a two-step explicit Runge–Kutta time integration scheme instead of first-order accurate Euler integration. Moreover, Roe's flux-difference split scheme is implemented for the cell interface fluxes, and a MUSCL extrapolation approach is further combined for a higher spatial accuracy. The method thereby yields second-order accurate results in both space and time at smooth parts of the flow, whereas it still keeps first-order accuracy at discontinuities such as shock waves. However, because numerical diffusion errors at discontinuities propagate throughout the flowfield, one can expect at best that the result have global first-order accuracy.[31] A more detailed discussion on the spatial and temporal accuracy of this method can be found by Kim.[32]

III. Geometry Configuration and Computational Setup

Figure 1 is a schematic of the variable cross section chamber and the simple tube. The variable cross section chamber has a main chamber with an internal radius of 120 mm and a length of 200 mm, whereas the small tubes arranged on both sides of the main chamber have the same internal radius of 20 mm and lengths of 200 mm. The simple tube has a 20 mm internal radius. The total length of the two channels is 800 mm. Each of the channels has the left end closed and the right opened.

A one-shot detonation process is considered. The channels are initially filled with a homogeneous stoichiometric hydrogen–air mixture at ambient condition (0.101325 MPa and 298.15 K). The detonation processes are initiated inside each channel near the closed end. The detonation products expand from the channels to the surrounding air directly. For both the compared cases, slip conditions are considered on the closed end-wall and the chamber surface. At the flow outlet boundary, that is, right-hand section, atmospheric conditions are implemented for each case. The flow solver time step is set at 10^{-7} s in all of the computations.

For the variable cross section chamber case, the different parts of the computational domain are meshed with structured grids, which are not all identical, whereas for the simple tube case, the computational domain is meshed with identically structured grids. A mesh convergence test is performed by trial and error to determine the proper mesh size to ensure accurate resolution of the physical process. Because detonation in the variable cross section chamber case will show more complicated flow features and, hence, is deemed to be more sensitive to mesh size than in the simple tube, the mesh convergence test has been done only for the variable cross section chamber case. The same configuration and parameters are used as earlier described. Four different mesh designs, namely, the computation domain meshed by 60×1600, 30×400, 30×300, and 25×200 cells, respectively, are examined. Figure 2 shows the temporal evolution of detonation pressure and temperature recorded at location 2 shown in Fig. 1 for these mesh designs. Figure 3 shows the distributions of pressure and temperature along the centerline of the chamber recorded at $t = 0.2$ ms. The convergence trend can be seen clearly from Figs. 2 and 3. The results of the mesh of 30×400 cells almost converged to the mesh of 60×1600 in both temporal variations and spatial distributions of detonation parameters. When we take into account accuracy as well as efficiency in choosing the mesh size, the mesh design of 30×400 cells is reasonable and is chosen for our current simulations.

The mesh size as chosen as described has a horizontal grid spacing of 2 mm. As has been shown in our earlier mesh convergence

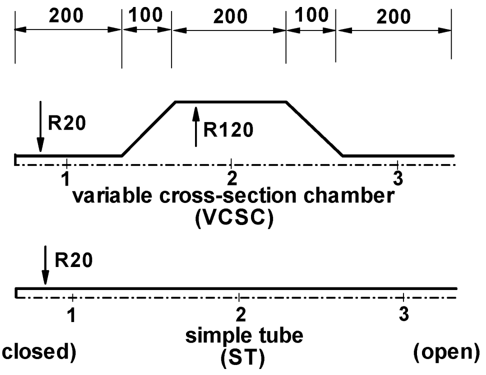

Fig. 1 Schematic of VCSC and ST: 1, 2, and 3 are horizontal locations used for displaying data of interest (dimensions in millimeters).

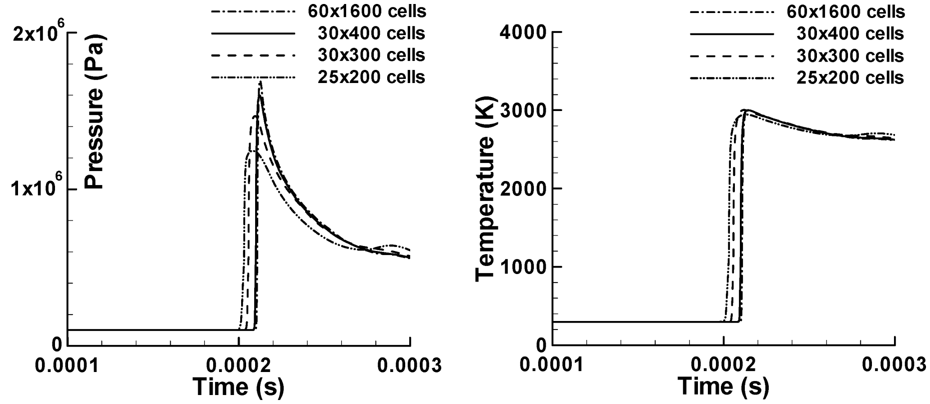

Fig. 2 Temporal evolution of the detonation parameters from different mesh designs.

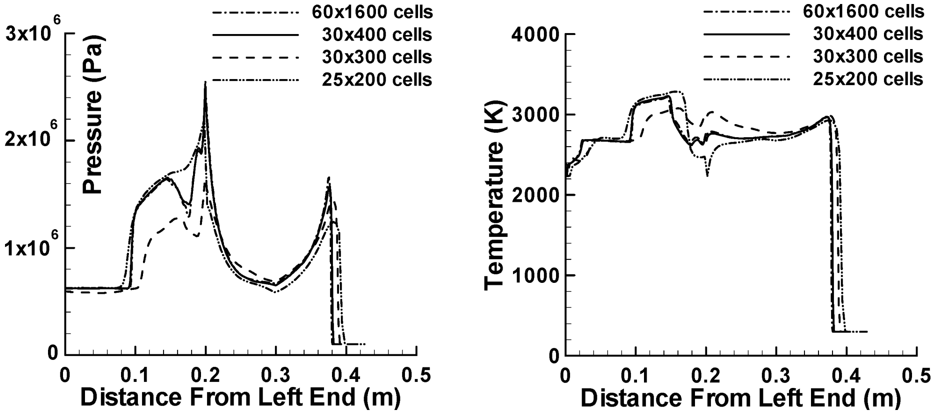

Fig. 3 Distribution of detonation parameters from different mesh designs.

experiment and in a similar study by Kim,[32] with this mesh size the adopted method can well capture the reaction equilibrium results of a detonation wave. Such a grid scale, however, may be too coarse to resolve the finer spatial detonation features. For example, if we intend to observe detailed detonation structures, an important characteristic that is needed to resolve may be the induction layer, a very small zone with no heat release between the shock front and the follow-up reaction area. For the stoichiometric hydrogen–air mixture in our current study, that induction zone length can be as small as 0.15–0.2 mm (Ref. 33). This implies that a mesh with 300×4000 cells or more will be necessary if this layer is to be resolved exactly. With the chosen numerical method and the existent computational source, the simulation on this mesh size will result in an extraordinarily time-consuming effort. Nevertheless, the present study focuses attention on the large-scale features of detonation waves from an applied perspective, such as the behavior of detonation initiation and propagation, the induced wave interactions, and the propulsive performance. The selected mesh size is thereby considered to be adequate for our current purpose.

The equilibrium hot spot ignition approach is applied to initiate a detonation wave from the closed end.[27] The success of a detonation initiation depends on the volume of the hot spot, and there is some critical volume of the hot spot for a specific detonation problem. (A detailed observation in this regard can be seen, for example, in Ref. 32.) For our current application, the volume of the hot spot is determined by trial and error to be as large as 5×10 cells for the selected mesh design, that is, 5 columns of cells adjacent to the closed end-wall and 10 rows of cells adjacent to the channel centerline are taken as ignition cells for both cases.

IV. Results and Discussion

A. Detonation Flowfield Features

The computed isobars at different times for the variable cross section chamber (VCSC) and the simple shock tube (ST) are presented in Fig. 4, which gives an overall view of the two detonation processes. Figure 4 shows that, as can be expected, the detonation process in the VCSC case reveals severe irregularity and nonuniformity in the flowfield behind the detonation wave due to wave diffraction and refraction at locations of area change, whereas the detonation process in the ST case appears relatively simple.

Both detonation waves propagate through identical tubes initially, and so there is no difference between them during this period. However, in the VCSC case, complex wave interactions occur as the primary detonation wave enters and exits the large chamber. The main features of the complex wave interactions were discussed in Ref. 26. Here, we focus our attention on a comparison between the VCSC and ST cases.

The intensity of a detonation wave front is examined using the pressure and temperature behind the front, as shown in Fig. 5. Figure 5 shows that the pressure and temperature of the detonation wave in the ST case asymptotically approaches a constant state, which is a little bit higher than the theoretical Chapman–Jouguet state ($p_{\mathrm{CJ}} = 1.586$ MPa, $T_{\mathrm{CJ}} = 2958$ K,$\rho_{\mathrm{CJ}} = 1.54$ kg/m^3, and $D_{\mathrm{CJ}} = 1977$ m/s) due to wave reflections within the tube, arising from the point of wave initiation.[27] In the VCSC case, these parameters show large variations. As the detonation wave exits the left small tube segment and enters the large chamber, the postdetonation pressure and temperature drop through the expansion process to values below the ST case, indicating a weakening of the wave. A slight recovery occurs during passage through the constant section of the large chamber. However, the wave strengthens rapidly as it enters the convergent portion of this chamber. The detonation wave then enters into the right small tube segment and propagates through it, sustaining a higher intensity.

The simulations for the VCSC and ST cases show that the detonation wave propagates at about the Chapman–Jouguet speed. However, the expansion and compression resulting from the cross-sectional changes in the VCSC case first decelerates and then accelerates detonation wave. This is evident in Fig. 4.

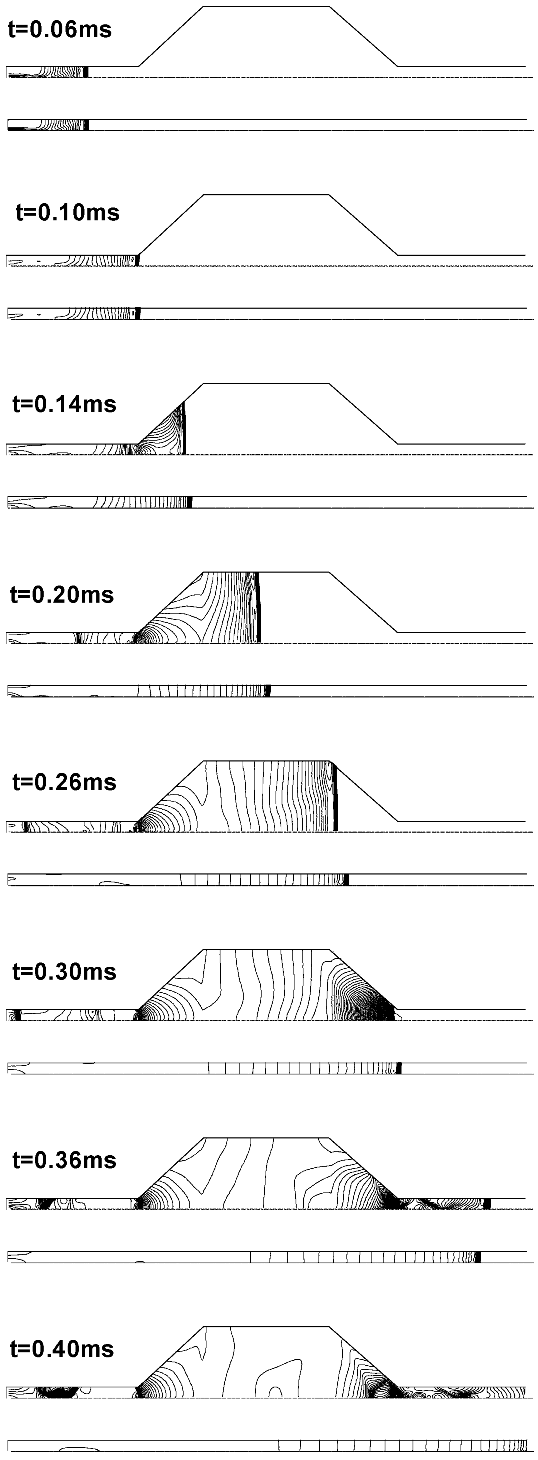

Fig. 4 Isobars of detonation processes obtained for the VCSC and ST cases.

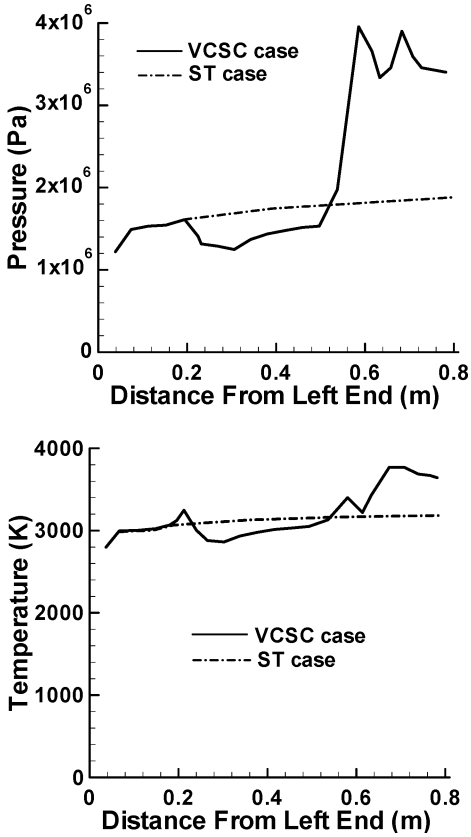

Fig. 5 Pressure and temperature at the detonation wave fronts as the waves propagate for the VCSC and ST cases.

The complexity of the postdetonation flowfield for the VCSC case is compared against the simpler ST case in Fig. 6, which shows the evolution of the pressure and temperature profiles along the centerline at various times. For a different viewpoint, the temporal evolution of the pressure and temperature at three different locations (Fig. 1) along the channel centerlines corresponding to the middle of the left small-tube segment, the main chamber, and the right-small tube segment in the VCSC case are shown in Fig. 7.

From Figs. 6 and 7, one further appreciates the complexity of the VCSC flow compared to the ST counterpart. The extreme parameters in the VCSC case can be many times higher than those in the ST case. The extreme parameters appearing in the right small-tube segment are chiefly caused by the convergent segment, as already mentioned and also shown in Fig. 5. However, for the extreme parameters that appear in the left small-tube segment, our simulation results showed that the reason is mainly attributed to reflection of the detonation wave at the exit of the small-tube segment. The reflected wave may further be reflected by the closed end-wall (giving rise to a secondary reflected wave), which then propagates to the right and suffers subsequent reflections at the area expansion. These reflection cycles gradually decline as the detonation flow evolves and the gaseous products drain out of the open section. Our computations can only completely record a cycle of the wave reflection process in the given computational period (0–0.6 ms). These reflected waves are apparent in Fig. 7 as pressure jumps at point 1. During the given time period, point 1 experiences three abrupt pressure increases caused by the detonation wave (DW) then a reflected wave (RW), and a further secondary reflected wave (SRW).

B. Propulsion Performance

The complexity of the DW and the postdetonation flowfield in the VCSC case affect the propulsion performance if it is configured for a PDE. For a generic detonation tube, the thrust produced by a detonation process can be calculated by the classical definition as

$$F(t) = \int_0^S \left[(p(t) - p_a) + \rho(t)u^2(t)\right] \mathrm{d}S \tag{6}$$

where p_a is the ambient pressure, and $p(t)$, $\rho(t)$, and $u(t)$ are the instantaneous pressure, density, and axial velocity acting on the wall, respectively. In Eq. (6), the integration area S is the area of the walls that the thrust acts on. For the ST case, the thrust is only exerted on the closed end-wall, so the preceding integration needs to be performed on that wall. However, for the VCSC case, the thrust production is more intricate than in the ST case. The thrust in this case is developed on three surfaces, as shown in Fig. 8. Besides the portion exerted on the closed end-wall denoted as F_1,

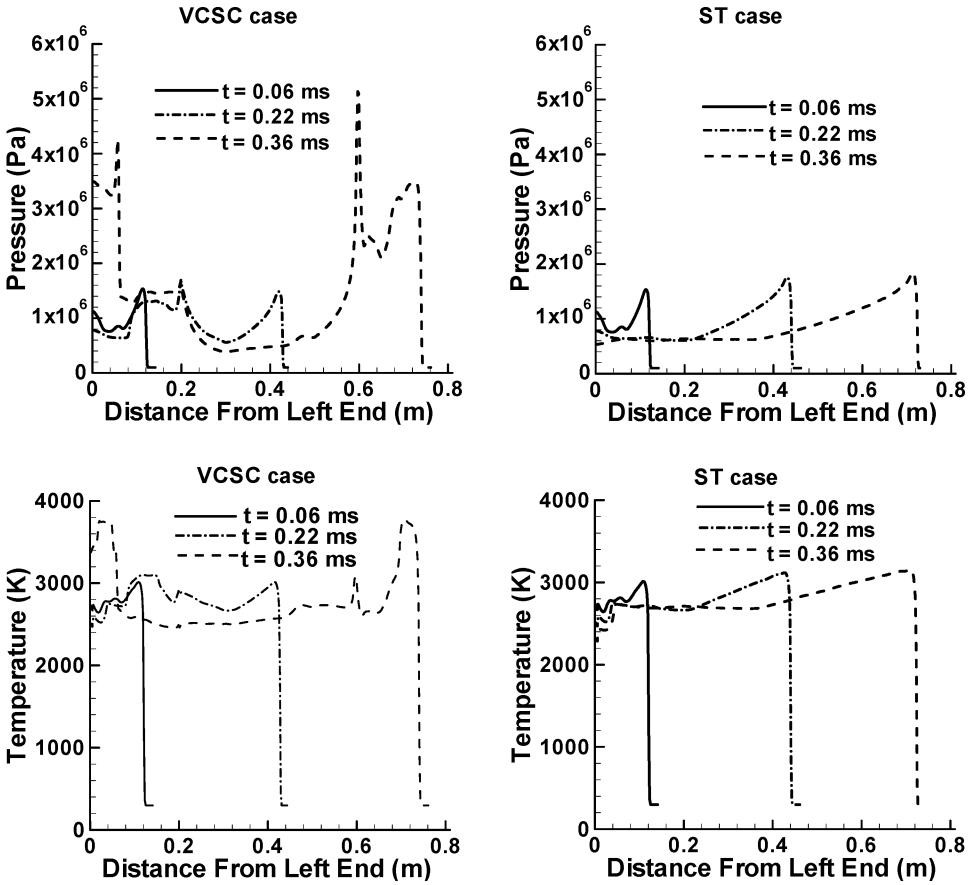

Fig. 6 Evolution of spatial distributions of pressure and temperature along the centerlines for the VCSC and ST cases.

thrust is also produced on both of the frustums. We denote the thrust components on the (left) divergent frustum as F_2 and on the (right) convergent frustum as F_3, respectively. Each thrust component in this case can be individually calculated with formula (6) on the associated integration areas.

Impulse is another parameter used to describe the performance of a propulsion system. The impulse can be obtained by integrating the thrust from zero to t as

$$I(t) = \int_0^t F(t)\,\mathrm{d}t \tag{7}$$

There are two specific impulse concepts that are also useful in evaluating propulsion performance. One is the reactant specific impulse that can be calculated, in our current application, from the relation

$$I_{\mathrm{sp}}(t) = I(t)/(\rho_0 V g) \tag{8}$$

where ρ_0 is the initial density of the reactant gas mixture in the detonation chamber, V is the volume of the chamber, and g is the Earth's sea-level gravitational acceleration. The other is the fuel-based specific impulse that can be defined as

$$I_{\mathrm{sp,f}}(t) = I(t)/(\rho_f V g) \tag{9}$$

where ρ_f is the initial density of the fuel gas (hydrogen in our case) in the detonation chamber.

The comparison of the propulsion performance in the current study is based on a one-shot detonation process. The computations were performed with a longer period (0–2.5 ms) to allow the detonation processes to exhaust to ambient conditions. The thrust for each of the detonation cases is shown in Fig. 9. In Fig. 9a, the thrust for the VCSC case is first shown together with its three components. For a clearer expression, the thrust of the ST case is shown in Fig. 9b together with F_1, exerted on the closed end-wall in the VCSC case. The results show that the detonation process in the VCSC case produces an astonishing thrust history compared with that in the ST case. This complicated behavior can further be understood through separately observing the histories of three components. The thrust F_1 exerted on the close end-wall depends, in principle, on the extreme parameter phenomenon existing near the end-wall of the small tube segment. The abrupt increase in F_1 is caused by the RW mentioned in Sec. IV.A. The force level thereafter remains high for a certain moment and eventually decays monotonically to zero. The behaviors of the other two forces, F_2 and F_3, are more complicated than that of F_1 and, thereby, may be the main reasons for the complicated thrust history of the VCSC case. These two forces are strongly dependent on the DW moving through the corresponding frustums. Moreover, the SRW mentioned in Sec. IV.A also has an evident effect on the forces. In particular, the force F_2 shows an abrupt increase as the DW passes the divergent frustum. Then the force F_2 experiences a small abrupt decrease followed by a gradual recovery that may be caused by the expansion effect of the frustum on the DW. The force F_2 then gradually increases due to the SRW passing through the frustum and, finally, decays monotonically to zero. Similarly, the force F_3 exerted on the surface of the convergent frustum has an abrupt decrease as the DW passes the associated frustum, yielding a negative thrust value. The force gradually increases until the SRW arrives and passes the frustum, resulting in an abrupt decrease of force, which thereafter monotonically increases to zero. In contrast, the thrust history in the ST case is typical in that it is extremely large at the moment of initiation, immediately reaches a plateau, and then decays monotonically. The average thrusts for the two cases are also calculated by

$$\bar{F} = \int_0^{t_{\max}} F(t)\frac{\mathrm{d}t}{t_{\max}} \tag{10}$$

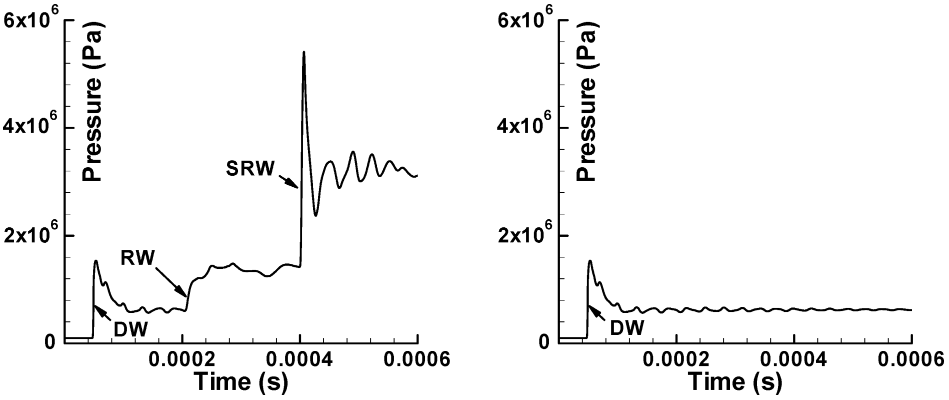

a) Point 1

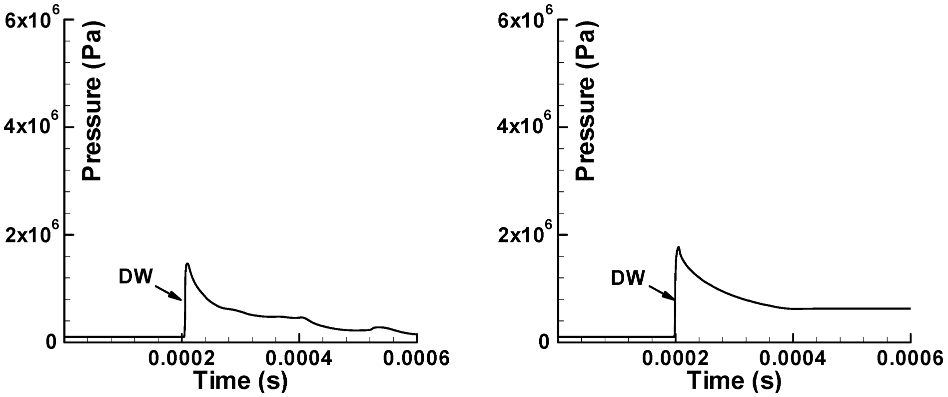

b) Point 2

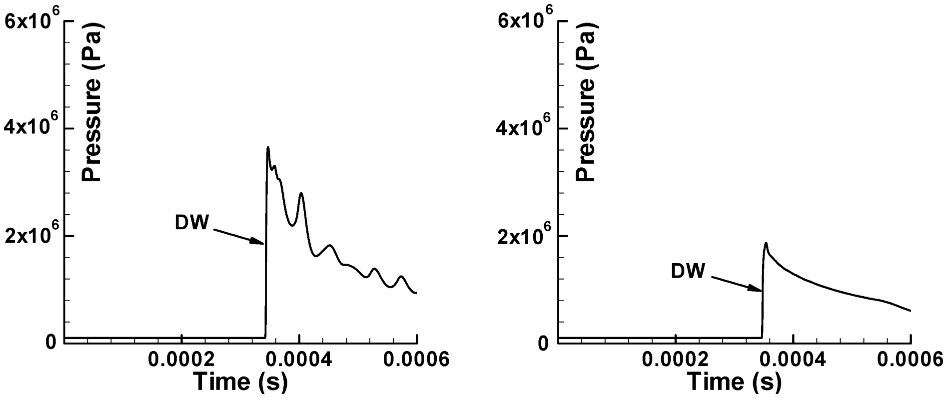

c) Point 3

Fig. 7 Temporal evolution of pressure at three locations (Fig. 1) along centerline of detonation channels: left-hand side, VCSC and right-hand side ST.

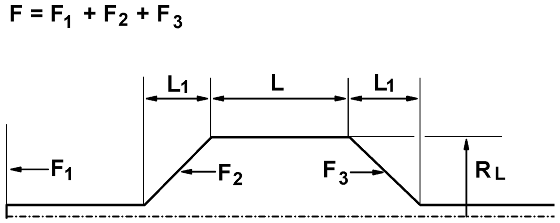

Fig. 8 Three thrust components and three geometric parameters for midchamber for VCSC case.

where $t_{\max} = 2.5$ ms. The average thrust in the VCSC case is 3038 N, that is, almost seven times of the average thrust of the ST case (441 N). This result shows the potential benefit of the variable section chamber for producing large thrust.

The various impulses for each of the detonation cases are shown in Fig. 10. The results may appear confusing at first. The detonation in the VCSC case produces a higher impulse value than that in the ST case. Nevertheless, for the two defined specific impulses, the detonation in the VCSC case has lower values, as compared with that in the ST case. Evidently, the larger channel volume in the VCSC case, about 13.4 times that of the ST case, means that more reactants are required in the former. Thus, there is a tradeoff between the higher thrust of the VCSC case and its larger consumption of reactants.

C. Midchamber Variations

A parametric study of the midchamber geometry for the VCSC case was performed. The midchamber's geometry can be described by three parameters, namely, the frustum length L_1, the primary length L, and the primary radius R_L, as shown in Fig. 8. To observe the sensitivity of each parameter on the associated detonation process, each parameter is allowed to vary independently from the baseline values of $L_{10} = 100$ mm, $L_0 = 200$ mm, and $R_{L0} = 120$ mm. The length L_1 takes on two additional values of 0.8 L_{10} and 1.2 L_{10}; similarly, L takes on 0.8 L_0 and 1.2 L_0. The radius R_L takes on the additional values of 0.6 R_{L0} and 0.8 R_{L0} to ensure that the selected mesh dimension in the radial direction remains small. The

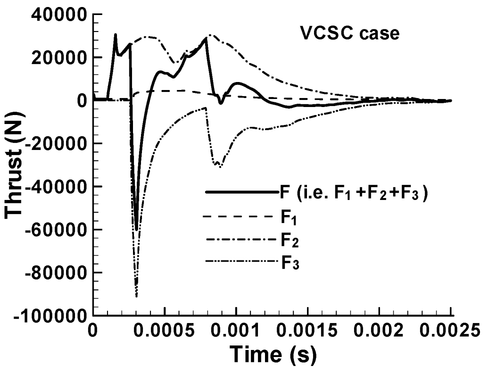

a) $F=F_1+F_2+F_3$

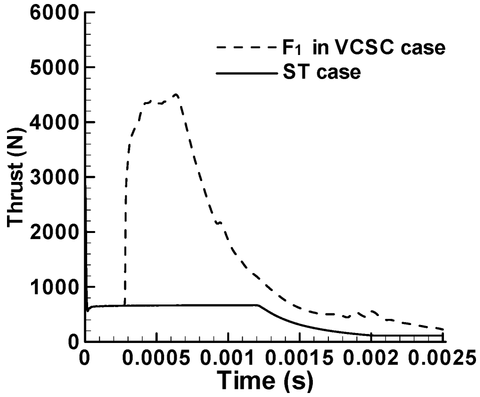

b) Thrust exerted on end-wall of ST and VCSC

Fig. 9 Thrust obtained from simulation of DW for VCSC and ST cases.

total length of the detonation chamber and the internal radii of the two small tubes are kept at their baseline values. Therefore, the length of the small tubes may vary when one of the midchamber dimensions changes. The detonative flow in these six new VCSC configurations were simulated with the same method and conditions described earlier. The computations were performed for the time period of 0–2.5 ms. As already discussed for the baseline case, the ensuing flowfield is extremely complex. Only a summary of the results are presented.

1. Flowfield Features

The waves that occur in the present VCSC case possess very intricate propagation and interaction characteristics. To extract the main features of the detonation processes from the different geometries, attention is focused on the early simulation period (0–0.6 ms). The three data points at the midpoints of the three tubes (as shown in Fig. 1) are still used to probe the features of the detonation processes. The temporal evolution of pressure recorded at the three locations during the detonation processes in the baseline and various geometries are shown in Figs. 11a–11c for variations in L_1, L, and R_L, respectively. The results show that the geometric variations have a more serious influence in the flow in the leftmost tube than elsewhere.

In the leftmost tube, a change of geometric parameters first affects the starting time of the RW. This change is attributed to a change of the leftmost tube length. Because the exit of this tube is where the RW is initiated by the DW, the RW will be initiated earlier if this tube is shorter and vice versa. The influence of L_1 and L on the wave reflection in the small tube is clearly seen in Figs. 11a and 11b. The variation of R_L does not affect tube length. Therefore, the waves for the different diameters of the midchamber are nearly coincident, as can be seen in Fig. 11c.

The different times that the RW in the leftmost tube is initiated for the different lengths of the midchamber affect the propagation of the SRW. Undoubtedly, the variations of the starting time produced from the different geometries consequently make the waves reach and further reflect the closed end-wall at different times, thereby causing the SRW to propagate at different time intervals. Moreover, a change in R_L causes a more significant change in the strength of the RW in the leftmost tube (point 1 in Fig. 11c). The different wave strengths then cause the SRW to propagate at different speeds, again as can be seen in Fig. 11c. This effect should also be present with changes in L_1 and L, because the reflected wave strength will be different. However, in our simulation results, the effect of L_1 and L on the reflected wave strengths appears to be weak.

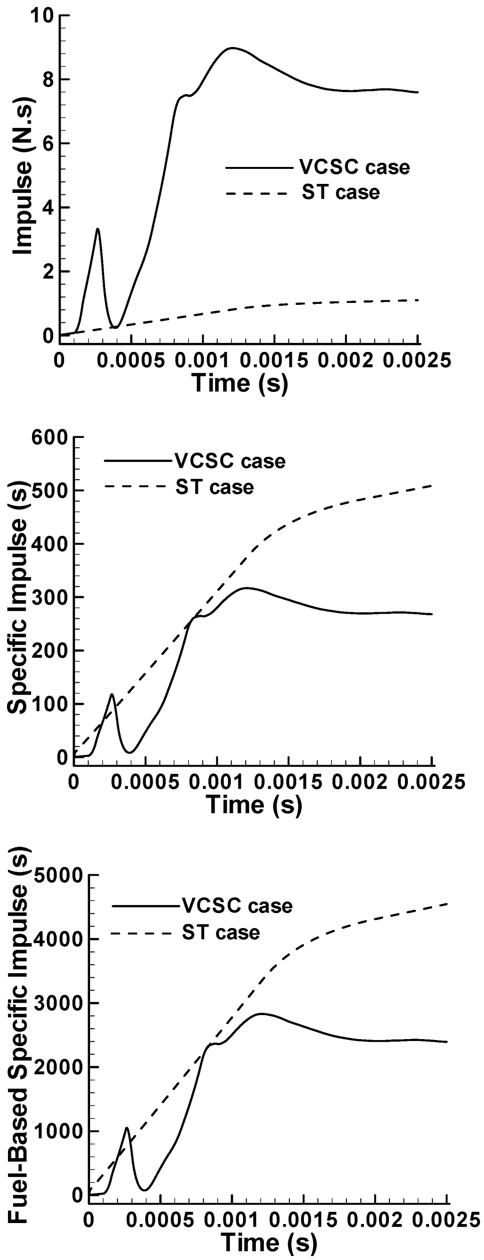

Fig. 10 Impulse obtained from simulation of DW for VCSC and ST cases.

Further observations can also be made about the leftmost tube. First, increasing L_1 or L is beneficial in obtaining a more stable and an increased average postwave performance especially for the SRW. An increase of R_L increases the postwave performance. However, there is a loss of performance stability. Second, an increase of L_1, L, or R_L tends to result in a higher peak value of the detonation parameters produced by the SRW in the tube.

The different geometries of the midchamber have a weak effect on the detonation processes within itself. Although the geometry

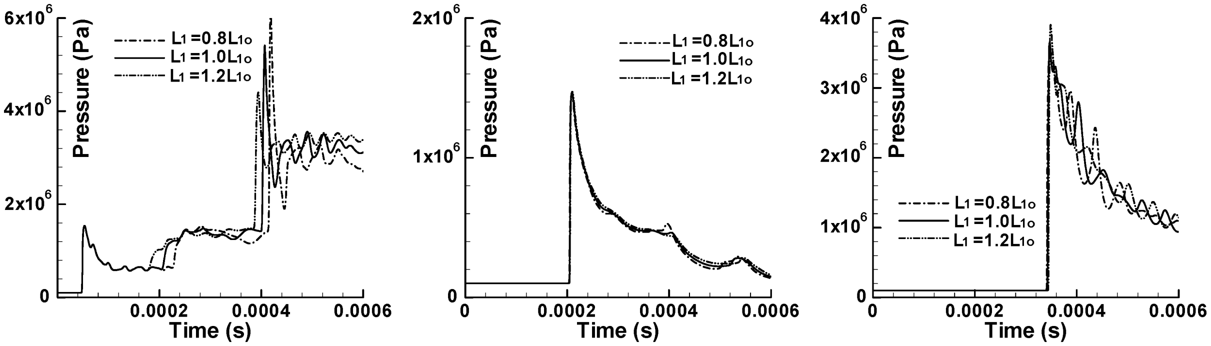

a) L_1 variation

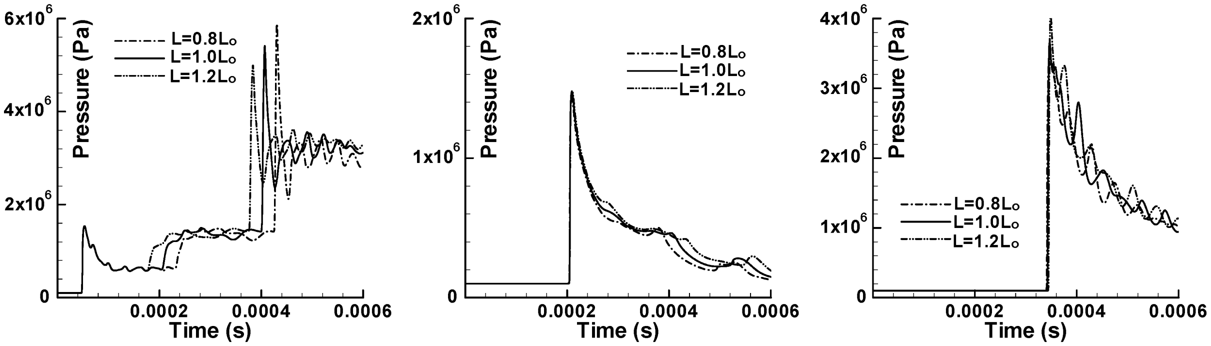

b) L variation

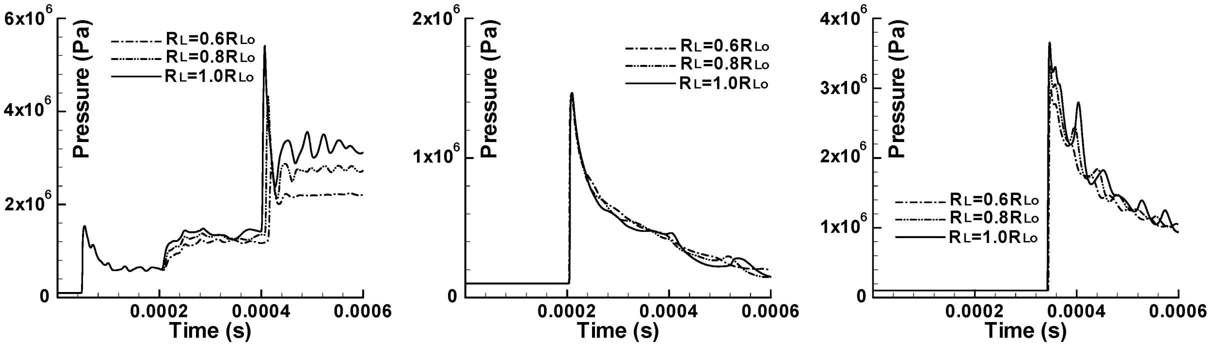

c) R_L variation

Fig. 11 Temporal evolution of pressure at three locations for different geometries of the midchamber for the VCSC case: left-hand side, point 1; middle, point 2; and right-hand side, point 3.

changes occur upstream of the data point (point 2), in all of the L_1, L, and R_L variations, the DW reaches the point at the same time for all of the selected geometries. The strengths of the detonation fronts also are the same.

For the rightmost tube, the changes of geometric parameters also affect to the DW propagation inside it, but not drastically. In all of the L_1, L, and R_L variations, the DW reaches the data point (point 3) almost simultaneously. However, the strengths of the detonation fronts vary depending on the values of the particular length scale. An increase of L_1, L, or R_L strengthens the front, presenting a higher detonation peak pressure as shown in Fig. 11.

2. *Propulsion Performance*

The thrusts obtained for the different midchamber geometries are shown in Fig. 12. Each thrust is the sum of three components (Fig. 8). The average thrusts over the computation period (0–2.5 ms) are also calculated and are shown in Fig. 13. In general, the temporal evolutions of the thrusts for all L_1, L, and R_L variations present some obvious differences only within the computation time before $t = 1.5$ ms. The thrust alters slightly when L_1 and L are varied but more so with R_L variation. These differences arise because, as can be anticipated, the former two situations keep the original midchamber diameter that defines the frustum surfaces for the two thrust components, whereas the third situation arises from changes in the diameter. Consequently, one finds that, when R_L varies, the thrust varies: The larger the diameter, the larger the thrust. From Fig. 13, we can see that the average thrusts change approximately in proportion with changes in L_1, L, and R_L. Among these three lengths, the thrust varies most with changes in the midchamber radius.

The irregular thrust performance can possibly clarified through an investigation of its three individual components. For brevity, only the thrust portion that acts on the left frustum, that is, F_2 is used as an example of the variations in all of the three components. Only a time interval of 0–0.6 ms is further investigated because this time interval shows the largest variations in thrust (Fig. 12). The thrust component F_2 for each of the different geometrical variations is shown in Fig. 14. Some observations from the results can be listed. When the frustum is elongated or shortened to fit a change of L_1 or L, the thrust starts

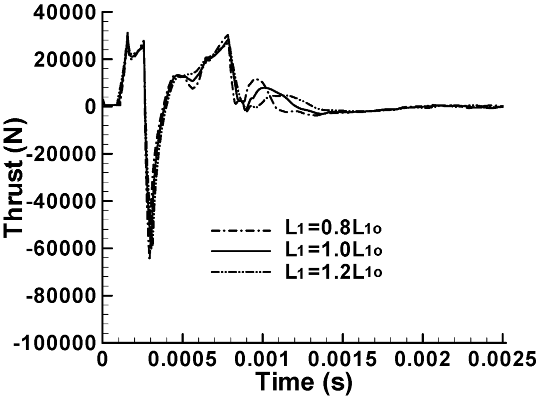

a) L_1 variation

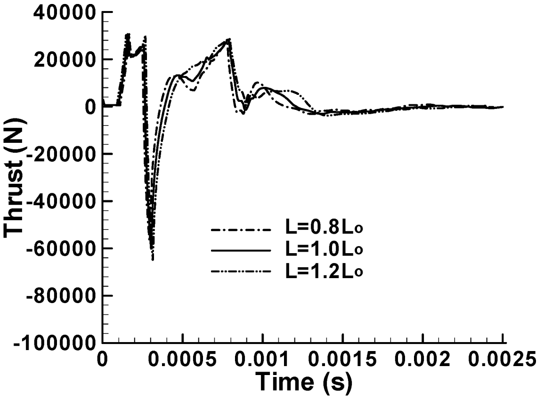

b) L variation

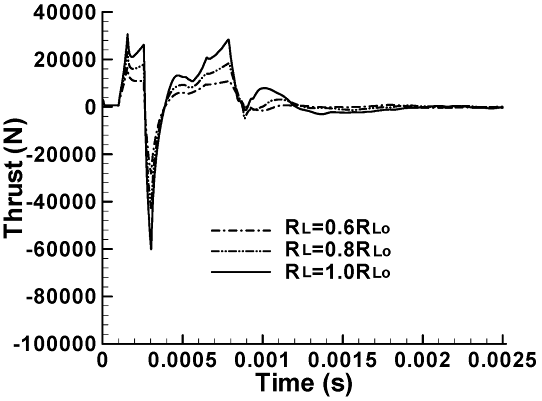

c) R_L variation

Fig. 12 Thrust for different geometries of midchamber for VCSC case.

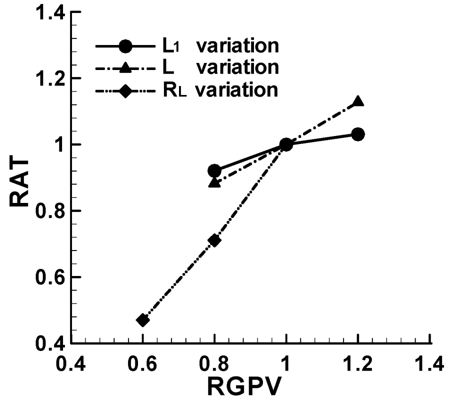

Fig. 13 Average thrust for different midchamber geometries for the VCSC case: relative average thrust (RAT) and relative geometric parameter variation (RGPV).

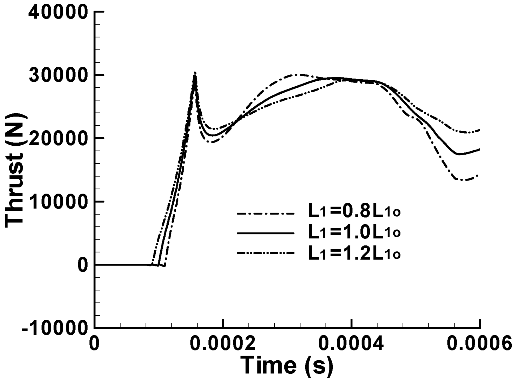

a) L_1 variation

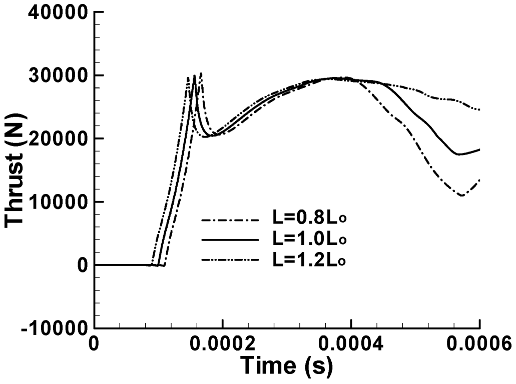

b) L variation

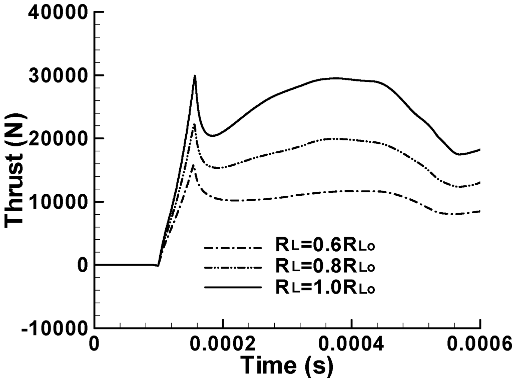

c) R_L variation

Fig. 14 Thrust component F_2 that is, component acting on the left frustum for different midchamber geometries, VCSC case.

to act on the surface earlier or later. The thrust peak appears when the DW exits the frustum. On the other hand, the peaks chiefly depend on the related exit diameter, or equivalently, the diameter of the midchamber. As a result, in the L_1 variation situation there is an identical peak, in the L variation situation there are three peaks that are almost in the same altitude, and in the R_L variation situation there are three peaks that are with evident different altitudes. In addition, a larger value of L_1 or L is advantageous to obtain a stable and sustainable performance for this thrust component, whereas a larger value of R_L is useful for obtaining higher thrust, however with a loss of stability and sustainability of this thrust component.

Finally, the impulses and specific impulses obtained for the different geometries are presented in Fig. 15. The changes of the selected geometric parameters can produce very different impulses. However, the specific impulses from the different geometries appear to plateau to approximately the same value (right-hand side of Fig. 15). This means that the specific impulse performance of the detonation process in the selected VCSC cases cannot be improved through changing those midchamber geometric parameters within the chosen ranges.

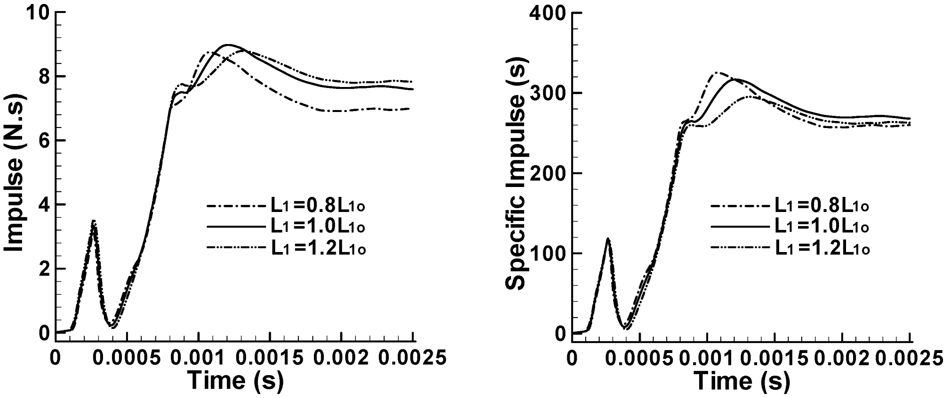

a) L_1 variation

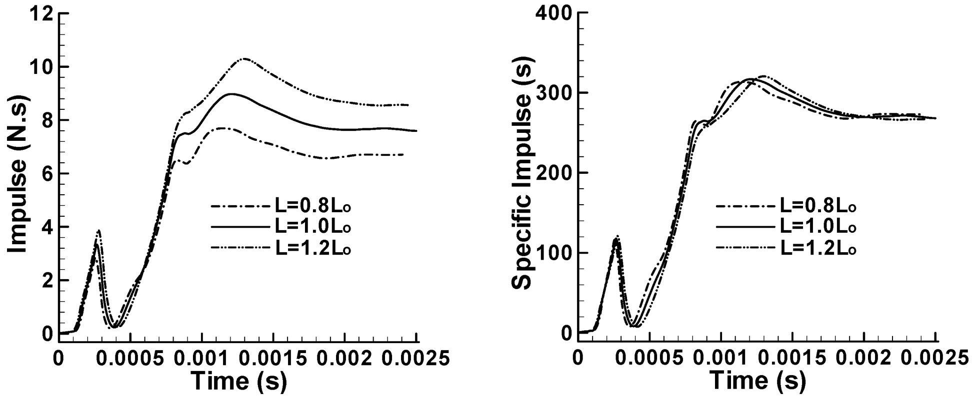

b) L variation

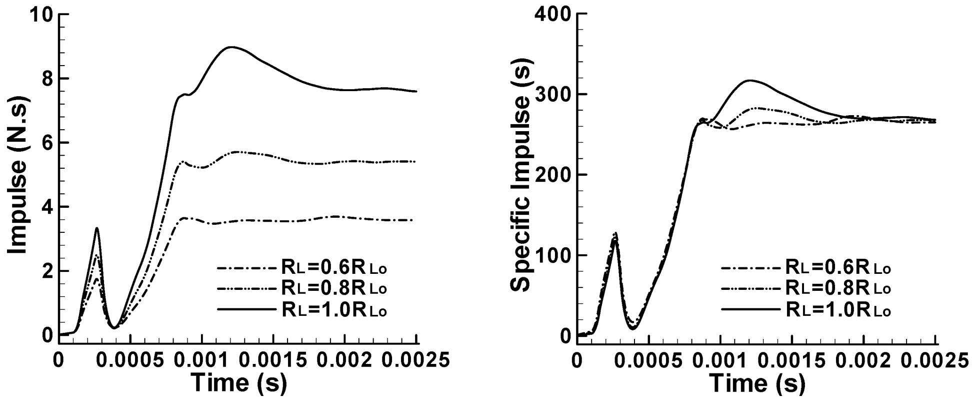

c) R_L variation

Fig. 15 Impulse and specific impulse for different midchamber geometries, VCSC case.

V. Conclusions

A comparison study was performed on the detonations occurring in a VCSC and a constant cross section tube by numerical simulations. A five-species and two-step reaction mechanism was adopted to model the thermochemistry of the detonation processes. A time-accurate and finite volume-based method was used in the simulations. The obtained results revealed that the detonation in a VCSC is much more complicated than that in the simple tube. The propulsion performance of the detonations in the two configurations was also compared. A VCSC can produce extreme flowfield parameters and, hence, offer a possibility for designing a PDE to have a much high-propulsion performance than a conventional PDE. An additional parameter study is also implemented for the VCSC and the sensitivity tendencies of the detonation processes to some geometric variations are presented.

Acknowledgments

The authors would like to thank the anonymous reviewers for their valuable comments on the paper. Particular thanks are due to J. Powers, Associate Editor of the journal, for his many constructive suggestions.

References

[1] Kailasanath, K., “Recent Developments in the Research on Pulse Detonation Engines,” *AIAA Journal*, Vol. 41, No. 2, 2003, pp. 145–159.

[2] Eidelman, S., Grossmann, W., and Lottati, I., “Review of Propulsion Application and Numerical Simulations of the Pulsed Detonation Engine Concept,” *Journal of Propulsion and Power*, Vol. 7, No. 6, 1991, pp. 857–865.

[3] Roy, G. D., “Practical Pulse Detonation Engines—How Far are They?” International Symposium on Air Breathing Engines, ISABE Paper 2001-1170, Sept. 2001.

[4] Litchford, R. J., “Development of Gas-Fed Pulse Detonation Research Engine,” AIAA Paper 2001-3814, July 2001.

[5] Cooper, M., Jackson, S., Austin, J., and Wintenberger, E., “Direct Experimental Measurements for Detonations and Deflagrations,” *Journal of Propulsion and Power*, Vol. 18, No. 5, 2002, pp. 1033–1041.

[6] Schauer, F., Stutrud, J., and Bradley, R., “Detonation Initiation Studies and Performance Results for Pulsed Detonation Engine Applications,” AIAA Paper 2001-1129, Jan. 2001.

[7] Hoke, J., Bradley, R., Stutrud, J., and Schauer, F., “Integration of a Pulsed Detonation Engine with an Ejector Pump and with a Turbo-Charger as Methods to Self-Aspirate,” AIAA Paper 2002-0615, Jan. 2002.

[8] Schauer, F., Bradley, R., and Hoke, J., “Interaction of a Pulsed Detonation Engine with a Turbine,” AIAA Paper 2003-0891, Jan. 2003.

[9] Hayashi, A. K., and Fujiwara, T., “Recent Progress of Japanese PDE Research,” AIAA Paper 2002-0475, Jan. 2002.

[10] Fan, W., Yan, C. J., Huang, Q., and Zhang, L. X., “Experimental Investigation on Two-Phase Pulse Detonation Engine,” *Combustion and Flame*, Vol. 133, No. 4, 2003, pp. 441–450.

[11] Wu, Y. H., Ma, F. H., and Yang, V., “System Performance and Thermodynamic Cycle Analysis of Airbreathing Pulse Detonation Engines,” *Journal of Propulsion and Power*, Vol. 19, No. 4, 2003, pp. 556–567.

[12] Wintenberger, E., Austin, J. M., Cooper, M., Jackson, S., and Shepherd, J. E., “Analytical Mode for the Impulse of Single-Cycle Pulse Detonation Tube,” *Journal of Propulsion and Power*, Vol. 19, No. 1, 2003, pp. 22–38.

[13] Wintenberger, E., and Shepherd, J. E., “The Performance of Steady Detonation Engines,” AIAA Paper 2003-0714, Jan. 2003.

[14] Li, C., and Kailasanath, K., “Detonation Transmission and Transition in Channels of Different Sizes,” *Proceedings of the Combustion Institute*, Vol. 28, Pt. 1, 2000, pp. 603–609.

[15] Kailasanath, K., Patnaik, G., and Li, C., “The Flowfield Performance of Pulse Detonation Engines,” *Proceedings of the Combustion Institute*, Vol. 29, Pt. 2, 2002, pp. 2855–2862.

[16] Li, C. P., and Kailasanath, K., “Partial Fuel Filling in Pulse Detonation Engines,” *Journal of Propulsion and Power*, Vol. 19, No. 5, 2003, pp. 908–916.

[17] Ebrahimi, H. B., and Merkle, C. L., “Numerical Simulation of a Pulse Detonation Engine with Hydrogen Fuels,” *Journal of Propulsion and Power*, Vol. 18, No. 5, 2002, pp. 1042–1048.

[18] Kawai, S., and Fujiwara, T., “Numerical Analysis of First and Second Cycles of Oxyhydrogen Pulse Detonation Engine,” *AIAA Journal*, Vol. 41, No. 10, 2003, pp. 2013–2019.

[19] Mawid, M. A., Park, T. W., Sekar, B., and Arana, C., “Application of Pulse Detonation Combustion to Turbofan Engines,” *Journal of Engineering for Gas Turbine and Power*, Vol. 125, Jan. 2003, pp. 270–283.

[20] He, X., and Karagozian, A. R., “Numerical Simulation of Pulse Detonation Engine,” *Journal of Scientific Computing*, Vol. 19, Nos. 1-3, 2003, pp. 201–224.

[21] Kailasanath, K., “A Review of PDE Research—Performance Estimates,” AIAA Paper 2001-0474, Jan. 2001.

[22] Kailasanath, K., “Review of Propulsion Applications of Detonation Waves,” *AIAA Journal*, Vol. 38, No. 9, 2000, pp. 1698–1708.

[23] Baklanov, D. I., Gvozdeva, L. G., and Scherbak, N. B., “Formation of High-Speed Gas Flow at Combustion in the Regime of Multi-Step Detonation,” *Gaseous and Heterogeneous Detonations, Science to Application*, edited by G. Roy, S. Frolov, K. Kailasanath, and N. Smirnov, ENAS Moscow, 1999, pp. 141–152.

[24] Baklanov, D. I., and Gvozdeva, L. G., “Nonstationary Processes During Propagation of Detonation Waves in Channels of Variable Cross Section,” *High Temperature*, Vol. 33, No. 6, 1995, pp. 955–958.

[25] Baklanov, D. I., and Gvozdeva, L. G., “The Effect of Additional Ignition on the Stability of Emergence of the Mode of Double Nonstationary Discontinuity in Combustors,” *High Temperature*, Vol. 34, No. 2, 1996, pp. 294–297.

[26] Fan, H. Y., and Lu, F. K., “Numerical Simulation of Detonation Processes in a Variable Cross-Section Chamber,” AIAA Paper 2004-2332, July 2004.

[27] Kim, H., Lu, F. K., Anderson, D. A., and Wilson, D. R., “Numerical Simulation of Detonation Process in a Tube,” *Computational Fluid Dynamics Journal*, Vol. 12, No. 2, 2003, pp. 227–241.

[28] Millikan, R. C., and White, D. R., “Systematics of Vibrational Relaxation,” *Journal of Chemical Physics*, Vol. 39, No. 12, 1963, pp. 3209–3213.

[29] Vincenti, W. G., and Kruger, C. H., *Introduction to Physical Gas Dynamics*, Krieger, Malabar, FL, 1977, p. 204.

[30] Rogers, R. C., and Chinitz, W., “Using a Global Hydrogen–Air Combustion Model in Turbulent Reacting Flow Calculations,” *AIAA Journal*, Vol. 21, No. 4, 1983, pp. 586–592.

[31] Gonthier, K. A., and Power, J. M., “A High-Resolution Numerical Method for a Two-Phase Model of Deflagration-to-Detonation Transition,” *Journal of Computational Physics*, Vol. 163, No. 2, 2000, pp. 376–433.

[32] Kim, H., “Numerical Simulation of Transient Combustion Process in Pulse Detonation Wave Engines,” Ph.D. Dissertation, Mechanical and Aerospace Engineering Dept., Univ. of Texas at Arlington, TX, May 2000.

[33] Lu, T., Law, C. K., and Ju, Y., “Some Aspects of Chemical Kinetics in Chapman–Jouguet Detonation: Induction Length Analysis,” *Journal of Propulsion and Power*, Vol. 19, No. 5, 2003, pp. 901–907.